An Activated TiC–SiC Composite for Natural Gas Upgrading via Catalytic Oxyhalogenation

Author(s):
Zichittella, Guido; Puértolas, Begoña; Siol, Sebastian; Paunović, Vladimir; Mitchell, Sharon; Pérez-Ramírez, Javier

Publication date:
2018-03-21

Permanent link:
https://doi.org/10.3929/ethz-b-000255689

Originally published in:
ChemCatChem 10(6), https://doi.org/10.1002/cctc.201701632

Funding acknowledgement:
156107 - Design of oxyhalogenation catalysts for hydrocarbon functionalization (SNF)

WILEY-VCH

Activated TiC-SiC Composite for Natural Gas Upgrading *via* Catalytic Oxyhalogenation

Guido Zichittella,[+[a]] Begoña Puértolas,[+[a]] Sebastian Siol,[[b]] Vladimir Paunović,[[a]] Sharon Mitchell,[[a]] and Javier Pérez-Ramírez*[[a]]

Abstract: Alkane oxyhalogenation has emerged as an attractive catalytic route for selective natural gas functionalization to important commodity chemicals, such as methyl halides or olefins. However, few systems have been disclosed to be active and selective in these reactions. Here, we identify a novel and highly efficient TiC-SiC composite for methane and ethane oxyhalogenation. Detailed characterization elucidates the kinetics and mechanism of the selective activation under reaction conditions to yield TiO_2-TiC-SiC. This catalyst outperformed bulk TiO_2, one of the best reported catalysts, reaching up to 85% selectivity and up to 3 times higher titanium-specific space-time-yield of methyl halides or ethylene. This was attributed to fact that the active TiO_2 phase generated *in situ* is embedded in the thermally conductive SiC matrix, facilitating heat dissipation thus improving selectivity control.

Introduction

The selective activation of the inert C−H bonds in methane and ethane, the principal components of natural gas, is one of the key challenges in catalysis research.[1-3] As abundant resources, these alkanes offer a huge potential for the manufacture of higher value chemicals and fuels. Nevertheless, over 30% of the world's natural gas is trapped in small basins and/or in remote areas, where its valorization *via* established technologies such as energy-intensive steam reforming or steam cracking is not economical.[4-7] Consequently, less than 10% of the global annual gas production is currently used for the manufacture of commodities, while *ca.* 3.5%, a share which is worth *ca.* 13 billion USD, is flared at oil and gas fields or refineries.[8,9] Over the last decades, alternative alkane activation routes, including the oxidative coupling and partial oxidation of methane[10] jointly with the partial oxidation[11,12] and oxidative dehydrogenation[13,14] of ethane to targeted products (*e.g.* carbon monoxide, methanol, or olefins), have been intensively studied. However, these paths typically suffer from limited selectivity, which stems from the fact that the intermediates and products are easier to activate than the alkane reactants.

Halogen-based processes find wide applications in the chemical industry for the efficient transformation of a carbon feedstock into valuable chemical intermediates.[7,15-17] In particular, oxyhalogenation, comprising the reaction of a hydrocarbon with O_2 and a hydrogen halide (HX, X = Cl, Br), has been demonstrated as a promising strategy for the selective functionalization of natural gas to yield methyl halides (CH_3X) or olefins. Various materials based on europium oxyhalides (EuOX), cerium oxide (CeO_2), and titanium oxide (TiO_2) have been identified to efficiently catalyze these reactions.[18-23] Particularly, in case of methane oxyhalogenation, the superior performance of these materials was related to their balanced redox properties, enabling the oxidation of HX, an important step for activity, while suppressing the oxidation of the desired methyl halides.[22] Still, the high reaction exothermicity imposes the practical challenge of designing catalysts capable of minimizing the formation of hot spots, which can detriment both the selectivity and stability. This issue could be addressed by embedding the active phase in a thermally conductive and chemically inert matrix such as silicon carbide. Recently, the controlled oxidation of a titanium carbide-silicon carbide (TiC-SiC) ceramic composite to TiO_2-SiC was shown to yield a high-performance photocatalyst for the degradation of 2-propanol,[23] as well as an efficient carrier for cobalt nanoparticles in Fischer-Tropsch synthesis, which was attributed to the combination of the thermal conductivity of SiC and the favorable cobalt-TiO_2 interactions.[25] The controlled transformation of TiC into TiO_2 in oxidative reaction environments could open further opportunities to develop efficient TiO_2-based catalysts in alkane oxyhalogenation reactions.

In this work, we demonstrate the high performance of TiC-SiC in the oxychlorination and oxybromination of methane and ethane to desired methyl halides or ethylene, respectively. Detailed characterization of the fresh and activated samples by means of X-ray diffraction (XRD), thermogravimetric analysis (TGA), transmission electron microscopy, and Raman, X-ray photoelectron (XPS), and ^{13}C and ^{29}Si nuclear magnetic resonance spectroscopies enabled elucidation of the kinetics and mechanism of the selective activation of TiC-SiC under reaction conditions. The beneficial impact of the intimate interaction between Ti-based phases and the SiC matrix is proven by comparison with physical mixtures and bulk TiO_2.

Results and Discussion

Characterization of TiC-SiC

The bulk composition and porosity of TiC-SiC were assessed by X-ray fluorescence (XRF) and N_2 sorption analyses (**Table 1**). The results revealed a total titanium content of 16.0 wt.% and the typical surface area (83 $m^2\ g^{-1}$) and interparticle porosity (Supporting Information **Figure S1**) of this type of material. The

[a] G. Zichittella,[+] Dr. B. Puértolas,[+] V. Paunović, Dr. S. Mitchell, Prof. J. Pérez-Ramírez
Department of Chemistry and Applied Bioscience, ETH Zurich
Institute for Chemical and Bioengineering
Vladimir-Prelog-Weg 1, 8093 Zurich (Switzerland)
E-mail: jpr@chem.ethz.ch

[b] Dr. S. Siol
EMPA, Swiss Federal Laboratories for Materials Science and Technology
Überlandstrasse 129, 8600 Dübendorf (Switzerland)

[+] Equal contribution.

Supporting information for this article is given *via* a link at the end of the document.

Table 1. Composition and porosity of the TiC-SiC composite in fresh form and after activation in methane oxychlorination (MOC) and oxybromination (MOB), and in ethane oxychlorination (EOC), and oxybromination (EOB).

Sample	Ti content / wt.%	S_{BET} / $m^2\ g^{-1}$	V_{pore} / $cm^3\ g^{-1}$
Fresh	16.0	83	0.12
MOC	17.5	24	0.09
MOB	17.9	26	0.09
EOC	18.4	25	0.08
EOB	16.5	65	0.09

characteristic reflections of both TiC and SiC phases were observed by X-ray diffraction (**Figure 1a**). The inspection of the scanning transmission electron (STEM) micrographs coupled with energy-dispersive X-ray (EDX) mapping (**Figure 2**) verified the presence of the two phases, in which the TiC phase appeared embedded within the SiC matrix. The partial surface oxidation of both phases was evidenced, which was corroborated by the observance of the Raman band of the anatase phase of titania at 155 cm^{-1} (*vide infra* **Figure 5a**) with the diffraction peak of SiO_2 (**Figure 1a**). Additional evidences were provided by ^{29}Si magic angle spinning nuclear magnetic resonance (MAS NMR) and XPS spectroscopies, where the band corresponding to the presence of $Q(SiO_4)$ units at –110 ppm in the ^{29}Si MAS NMR spectrum (*vide infra* **Figure 6a**),[26] and SiO_2 and TiO_2 components in the Si 2*p* and Ti 2*p* XPS core level spectra (*vide infra* **Figure 5c**, Supporting Information **Figure S7**), respectively, were observed. To determine the evolution of the TiC and SiC phases in an oxidative environment, TGA in air together with temperature-programmed oxidation with oxygen (O_2-TPO) were conducted (**Figure 3**). The weight increase from *ca.* 600 K to 800 K along with the formation of CO_x species was ascribed to the partial transformation of TiC into TiO_2, which was completed at *ca.* 1000 K.[27] From *ca.* 800 K to 1000 K, a weight loss accompanied by the evolution of the *m/z* 28 and 44 signals was evidenced. This could be the result of the simultaneous oxidation of the remaining TiC and of the residual carbon in the composite that was not carburized completely during the synthesis[28] and/or of binders, such as methyl cellulose, polyvinyl alcohol, or polyethylene glycol among others that could have been added during the shaping process.[29] At temperatures higher than *ca.* 1000 K, the transformation of SiC into SiO_2 occurred consistent with the observed weight increase.

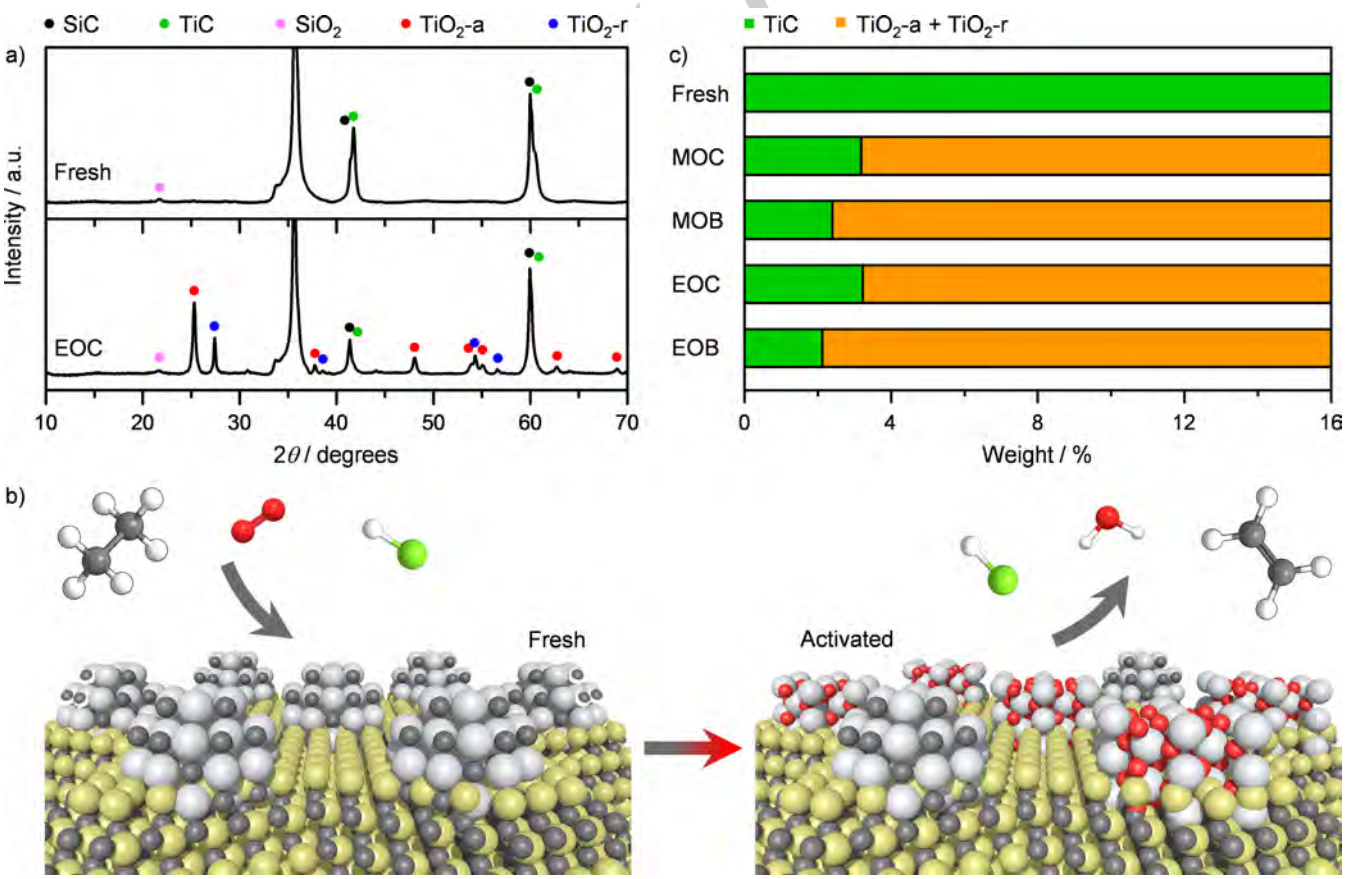

Figure 1. a) X-ray diffractograms of TiC-SiC in fresh form and after activation in EOC. The diffractograms of the samples after activation in MOC, MOB, and EOB are provided in **Figure S2** of the Supporting Information. **b)** Schematic representation of the activation of TiC-SiC into TiO_2-TiC-SiC in EOC. Color code: Si (yellow), C (dark gray), Ti (light gray), O (red), Cl (green), H (white). **c)** Quantification of the TiC and TiO_2 phases in the fresh and activated samples derived from TGA analysis. The TGA profiles are provided in **Figure S3** of the Supporting Information.

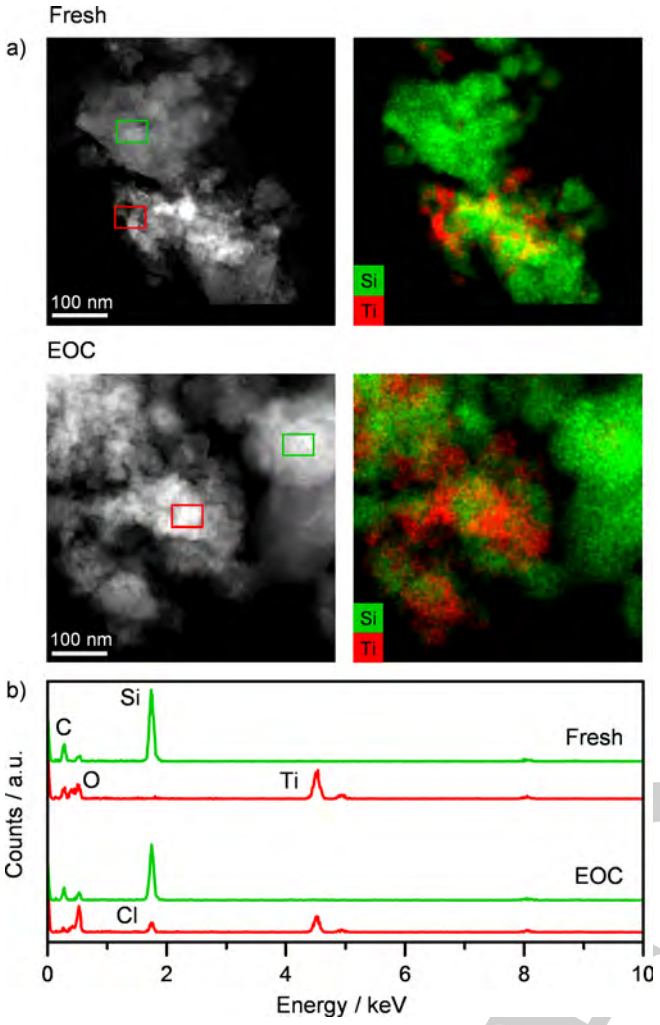

Figure 2. a) Scanning transmission electron micrographs (left) and corresponding elemental maps (right) of TiC-SiC in fresh form and after activation in EOC. **b)** EDX spectra corresponding to the boxed Si (green box) and Ti (red box) rich regions. The scanning transmission electron micrographs with corresponding elemental maps and EDX spectra of TiC-SiC after activation in EOB are provided in **Figure S4** of the Supporting Information.

TiC-SiC as catalyst for alkane oxyhalogenation

TiC-SiC was activated in methane and ethane oxyhalogenation under the same conditions previously reported by our group,[22,23] *i.e.* variable temperature (from 680 K to 850 K) and using a stoichiometric ratio of reactants (alkane:HX:O_2 = 6:6:3) in the inlet feed. The resulting material was active in all investigated reactions, as reflected by the rate of alkane *i* consumed (**Figure 4**). This ranged between 0.5 and 1.5 mol_{CH_4} h^{-1} mol_{Ti}^{-1} at 723 K and 850 K, respectively in methane oxychlorination (MOC), whereas a higher level of activity was attained when the activation was conducted under methane oxybromination (MOB) conditions (2.7 mol_{CH_4} h^{-1} mol_{Ti}^{-1} at 850 K). Similarly, the activation in ethane oxybromination (EOB) lead to improved performance compared to that attained in ethane oxychlorination (EOC), particularly at low temperatures, where the composite achieved a rate of 2.8 and 0.9 $mol_{C_2H_6}$ h^{-1} mol_{Ti}^{-1}, respectively, at 723 K, but became similar upon increasing the reaction temperature.

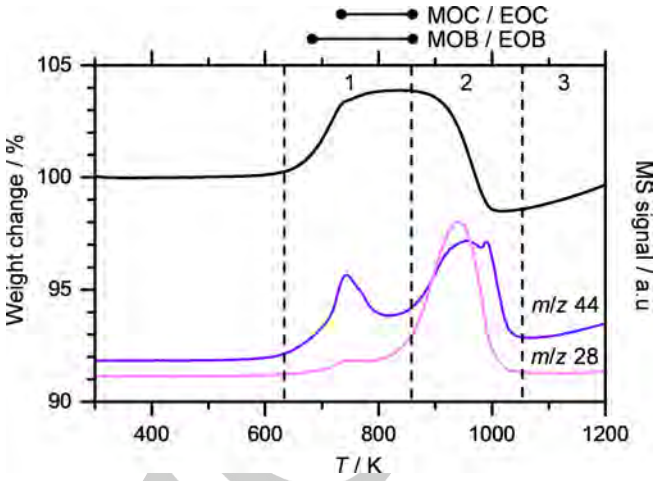

Figure 3. TGA analysis in air and CO_x evolution of TiC-SiC in fresh form. Regions 1, 2, and 3 represent the temperature windows where the following reactions take place: in Region 1, the oxidation of TiC to TiO_2 and CO_x occurs; in Region 2, the oxidation of the free carbon and binders that could be present in the sample to CO_x plus completion of the first reaction happen, and in Region 3, the oxidation of SiC to SiO_2 and CO_x takes place. Operating temperatures in the studied reactions are shown on top of the figure.

Although activation under oxybromination conditions resulted in superior activity for both C_1 and C_2 alkanes, the trend of the selectivity to the desired product for the individual alkanes is similar regardless of the halogen source. The main difference between oxybromination and oxychlorination reactions lied on the variation of the selectivity to the desired CH_3X or C_2H_4 with the temperature, which was more prominent in the former case. In particular, in MOC it decreased from 50% at 723 K to 40% at 850 K over the catalyst activated under these conditions (**Figure 4a**),[22] whereas the composite activated in MOB showed 85% selectivity to CH_3Br at the lowest temperature, which fell to 25% at 850 K. In both cases, CO is the major byproduct with a selectivity lower than 55% (Supporting Information **Figure S5**) over the MOC-activated catalyst and ≤ 60% at 850 K over the catalyst activated in MOB. On the other hand, for the samples activated in EOC and EOB, the selectivity to the desired C_2H_4 increased with the reaction temperature (**Figure 4b**). For the EOC-activated catalyst, C_2H_4 generation increased from 70% to 80%, whereas limited CO_x production was observed (S_{CO} ≤ 12% and S_{CO_2} ≤ 2%). This behavior was accompanied by a decrease in the selectivity to C_2H_5Cl ($S_{C_2H_5Cl}$ ≤ 20%; Supporting Information **Figure S5**), suggesting the occurrence of a consecutive oxychlorination-dehydrochlorination mechanism, in line with a recent study on olefin production *via* alkane oxychlorination.[23] In the case of the EOB-activated catalyst, a pronounced increase in the selectivity to C_2H_4 from 15% to 65% was evidenced, along with a decrease in CH_4 (S_{CH_4} ≤ 20%) and CO (S_{CO} ≤ 30%) generation.

Characterization of activated TiC-SiC

Table 1 summarizes the compositional and textural properties of activated TiC-SiC in methane and ethane oxyhalogenation. N_2 sorption results evidenced the partial sintering upon activation, as shown by the decrease in the surface area. The titanium loading was preserved and any halogenation of the surface was very limited as confirmed by the EDX spectra (**Figure 2** and

Supporting Information **Figure S4**). XRD and TGA analyses of the activated samples (**Figure 1** and Supporting Information **Figures S2** and **S3**) revealed the partial evolution of TiC into TiO_2 leading to TiO_2-TiC-SiC, as schematized in **Figure 1b**. This *in situ* formed TiO_2 phase was responsible of the reducibility properties of the catalysts (**Figure 5b**), which are essential in oxidation reactions. X-ray diffractograms evidenced the presence of different proportions of anatase and rutile phases depending on the reaction medium being anatase the main phase in all the activated samples (Supporting Information **Figure S2**). Although no changes were detected in the bulk by XRD analysis, XPS spectra revealed different Ti speciation on the catalyst surface depending on the activation conditions. In particular, Ti^{4+} species were present after activation under EOC and EOB conditions, and a higher contribution from Ti^{3+} was evidenced on the EOB-activated catalyst. The latter might be ascribed to the stronger reducing ability of HBr, as being observed in the oxidation of HBr to Br_2 over TiO_2 catalyst.[30] The recrystallization of the TiO_2 phase appeared to slightly increase the particle size compared to that of TiC. This was corroborated by the decrease in the interparticle porosity in the activated samples (Supporting Information **Figure S1**). In addition, the formation of TiO_2 particles of well-defined morphology that remained embedded within the SiC matrix was evidenced as displayed in the micrographs of **Figures 2** and Supporting Information **Figure S4**. The transformation of TiC into TiO_2 was also observed by XPS analysis, showing only TiO_2 on the surface of the activated catalysts (**Figure 5c**), and an increase in

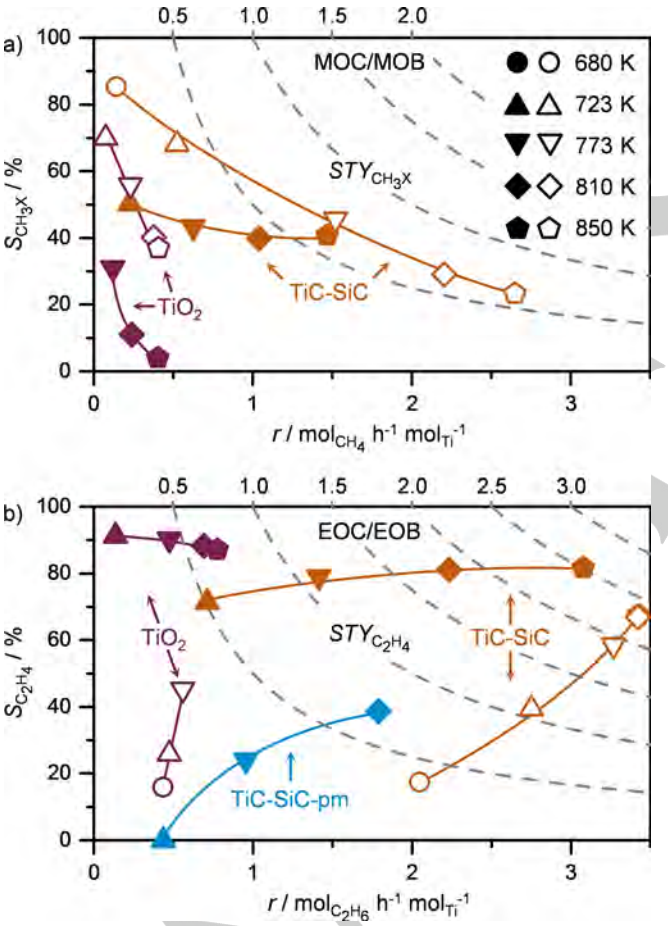

Figure 4. Selectivity to **a)** CH_3X or **b)** C_2H_4 as a function of the rate of alkane consumption in the oxychlorination (solid symbols) and oxybromination (open symbols) of methane (MOC/MOB) and ethane (EOC/EOB) over TiC-SiC and TiO_2. A comparison with a physical mixture of TiO_2 and SiC (TiO_2-SiC-pm) with the same Ti content (16 wt.%) is provided for EOC. The dashed gray lines indicate the space-time-yield of product j (j = CH_3X, C_2H_4) in mol_j h^{-1} mol_{Ti}^{-1} and the different symbols refer to the reaction temperature. The selectivity to remaining reaction products is provided in **Figures S5** and **S6** of the Supporting Information. Feed composition: alkane:HX:O_2:Ar:He = 6:6:3:4.5:80.5.

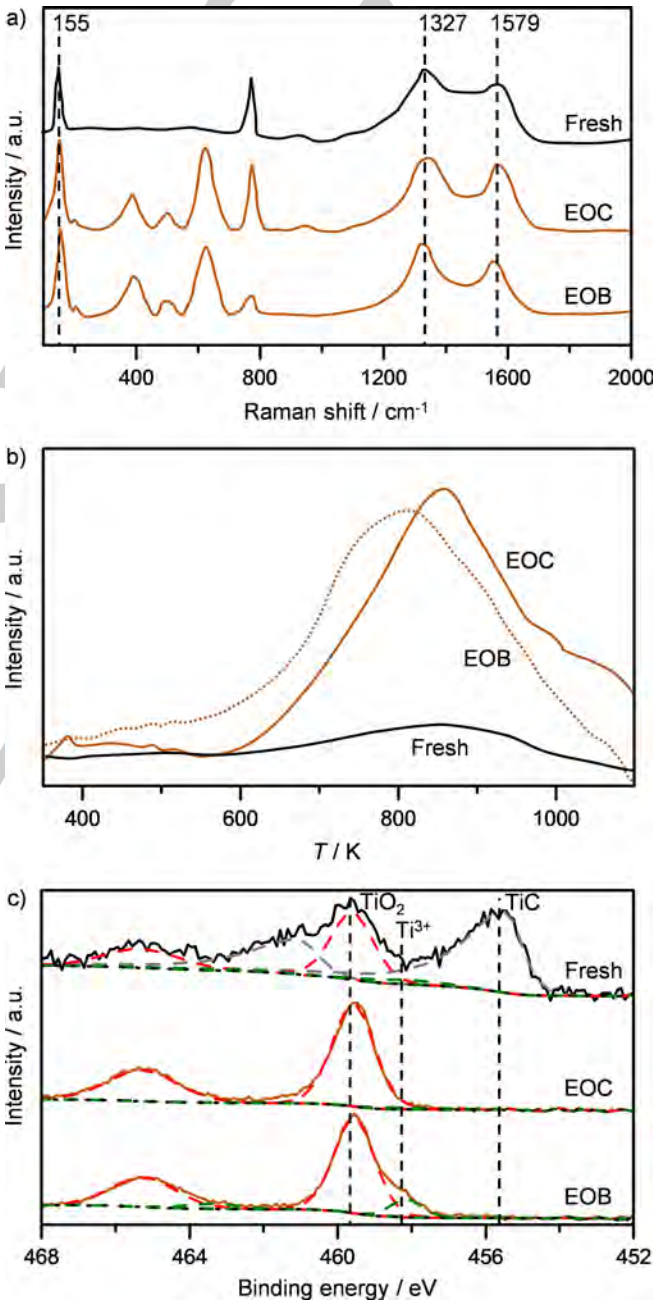

Figure 5. a) Raman spectra, **b)** temperature-programmed reduction with H_2 (H_2-TPR) profiles, and **c)** Ti 2*p* core level spectra of TiC-SiC in fresh form and after activation in EOC and EOB. The solid, dotted, and dashed lines represent the raw data, background, and fits of the different Ti 2*p* contributions, respectively. Si 2*p*, O 1*s*, and C 1*s* core level spectra are provided in **Figure S7** of the Supporting Information.

the elemental surface oxygen concentration after EOC (Supporting Information **Table S1**). On the other hand, analysis of the bulk material by TGA showed that a fraction of TiC remained unconverted after the reaction (**Figure 1c**) in accordance with the higher temperatures required for its complete transformation.[27] The remaining loading was *ca.* 3 wt.%, as derived from TGA analysis (Supporting Information **Figure S3**). The occurrence of TiC was also corroborated by Raman spectroscopy, where the characteristic bands of TiC at 1327 and 1579 cm^{-1} [31] were identified in the fresh sample and after activation in EOC and EOB (**Figure 5a**). Nevertheless, these bands can also be assigned to elemental carbon, coming either from the incomplete carburization of precursors in the fresh sample or from possible coke deposits on the activated catalysts. Accordingly, the TiC phase could not be detected by transmission electron microscopy, which suggests the presence of the unreacted TiC in the form of small nanoparticles well-dispersed in the SiC matrix.

The Si and C environments of the fresh and selected activated samples were assessed by ^{29}Si and ^{13}C MAS NMR spectroscopies, leading to similar results in all cases (**Figure 6**). The signal centered at 16 ppm in the ^{29}Si MAS NMR spectra with two additional contributions at 20 and 25 ppm corresponds to the presence of partly amorphous SiC phase that kept unaltered during the reaction.[32,33] The latter is corroborated by ^{13}C MAS NMR spectroscopy, which evidenced the occurrence of *sp* and sp^2 carbon associated to C≡C and C=C bonds, respectively with a chemical shift centered at 103 ppm in all the investigated samples. Together with the XRD analysis, which exhibited the characteristic diffraction peaks of the SiC phase (Supporting Information **Figure S2**), these results suggest the existence of crystalline domains dispersed in an amorphous matrix. The absence of additional bands at –5, –35, and –70 ppm (the latter not shown) in the ^{29}Si MAS NMR spectra discarded the formation of any bulk silicon oxycarbide phase, *i.e.* SiC_3O, SiC_2O_2, and $SiCO_3$, respectively.[34,35] On the other hand, the comparison of the signal at –110 ppm for the fresh and the activated samples revealed a small shift, which could be related to a possible oxygen redistribution during reaction. The intensity of this band evidenced a negligible increase upon activation, thus suggesting the stability of the SiC phase towards oxidation under activation conditions in line with the XRD, TGA, and O_2-TPO results (Supporting Information **Figure S2** and **Figure 3**). Assessment of the ^{13}C MAS NMR spectra (**Figure 6b**) also corroborated these findings, as the intensity of the band ascribed to SiC (20 ppm) remained identical in all cases. On the other hand, XPS analysis has shown the presence of SiO_2 that increased after activation in EOC and EOB (Supporting Information **Figure S7**), suggesting that SiC oxidation is limited to the surface of the catalyst.

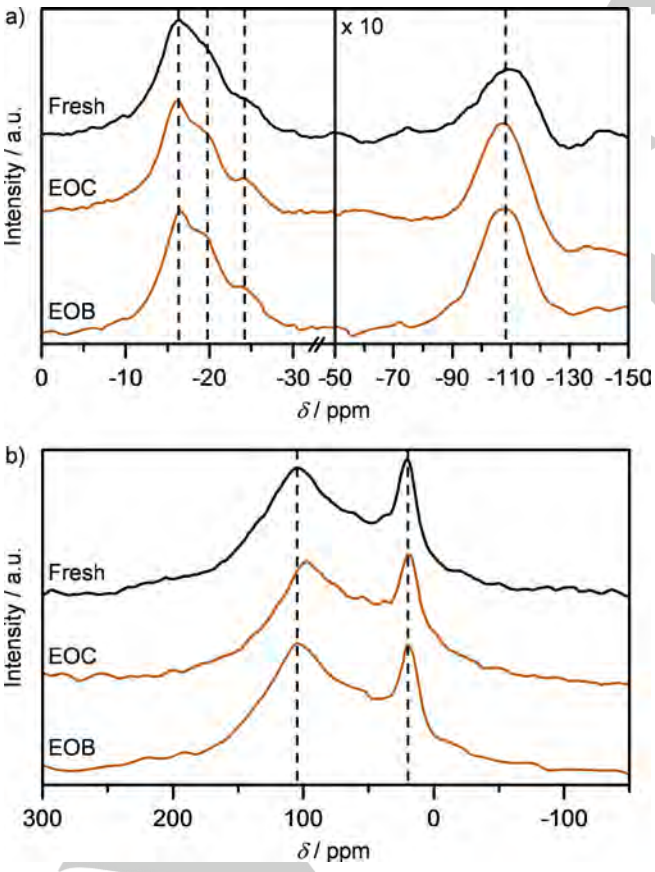

Figure 6 a) ^{29}Si and **b)** ^{13}C MAS NMR spectra of TiC-SiC in fresh form and after activation in EOC and EOB.

After identifying the morphological and structural properties of TiO_2-TiC-SiC that led to the observed performance, the kinetics of the activation process of TiC-SiC were elucidated in the oxidation of HCl (HCO) and HBr (HBO) to molecular chlorine and bromine, respectively. The selection of these reactions is based on two main reasons: (*i*) they have been suggested as important steps for the activity in methane oxyhalogenation,[22] and (*ii*) the absence of the alkane enables the decoupling of the impact of the halogen from that of the alkane on the activation mechanism. Assessment of the activation in HCO and HBO upon increasing the reaction temperature (**Figure 7a**) led to a final material similar to that attained after activation in alkane oxyhalogenation as evidenced by the similar distribution of the anatase and rutile phases of TiO_2 (Supporting Information **Figures S2** and **S8**), suggesting that the alkane does not play an important role in the catalyst transformation. Subsequent evaluation with time-on-stream (*tos*) at a constant reaction temperature, *i.e.* 810 K, under HCO and HBO conditions (**Figure 7b**) revealed a progressive transformation into TiO_2-TiC-SiC in both cases in parallel with the evolution of the activity. In particular, no activity was detected under HCO activation conditions within the first hour. After 2 h on stream, activation of the catalyst occurred as evidenced by the increase in the rate of chlorine production to 0.06 mol_{Cl_2} h^{-1} mol_{Ti}^{-1}, which remained constant for the successive 18 h. On the other hand, bromine production raised from 2.3 to 3.2 mol_{Br_2} h^{-1} mol_{Ti}^{-1} within the first 5 h on stream followed by a slight decrease in the activity that levelled off to 2.6 mol_{Br_2} h^{-1} mol_{Ti}^{-1} after 10 h on stream. Although the activity stabilized faster under HCO than under HBO conditions, the catalyst was more active in alkane oxybromination, as previously discussed (**Figure 4**), which might be related to the easier activation of HBr over the catalyst, as reported for TiO_2 in methane oxyhalogenation.[22] The activated

catalysts in HCO and HBO were characterized after 0.5, 5, and 20 h on stream. XRD analysis evidenced the formation of TiO_2 after 0.5 h on stream in both cases, being rutile the major phase (Supporting Information **Figure S9**). This contrasted the attained results for the activated samples in the temperature-ramping alkane oxyhalogenation and HX oxidation experiments where anatase was the most prominent phase. The observed difference could be ascribed to the fact that the transformation from anatase to rutile proceeded progressively with the temperature increase, whereas the activation of TiC into TiO_2 phases under HCO and HBO reaction conditions occurred at 810 K, where rutile is the thermodynamically favored phase.[36] Quantification of the evolution of TiC into TiO_2 in the samples by TGA analysis demonstrated the continuous transformation with *tos* in both reactions (**Figure 7c**). XPS analysis of the samples subjected to HBO revealed an increase in the SiO_2 component with increasing time, in agreement with the decrease of the SiC signal. In contrast, no significant changes are observed between the samples treated under HCO or HBO conditions (Supporting Information **Figure S11**). Contrarily to TGA analysis, no traces of the TiC phase are detected on the catalyst surface, thus suggesting the occurrence of TiC on the bulk of the catalyst. STEM coupled with elemental mapping of the activated samples after 0.5 h in HBO (Supporting Information **Figure S12**) confirmed the presence of TiO_2 in line with the XRD and TGA results. However, the TiC phase could not be detected as previously observed for the activated samples in alkane oxyhalogenation. In addition, TGA results elucidated the kinetics of activation of TiC into TiO_2, which was much faster under HCO than under HBO conditions. In the former reaction, no change in the TiC content (*ca.* 3 wt.%) was observed after 5 h on stream, whereas for the activation in HBO, the TiC loading in the composite decreased from 8 wt.% to *ca.* 3 wt.% between 5 h and 20 h on stream, respectively. These differences could be explained by the fact that bromine evolves much easier than chlorine from the TiO_2 surface,[22,37] resulting in much higher activity in HBO compared to HCO, which leads to higher oxygen consumption, and therefore slower kinetics of activation.

Comparison of TiC-SiC with benchmark catalysts in alkane oxyhalogenation

The performance of TiO_2-TiC-SiC was compared to that of bulk TiO_2, a benchmark oxyhalogenation catalyst.[21-23] In particular, we have used the anatase phase of TiO_2, as it was the main phase observed upon activation of TiC-SiC. Although rutile is the benchmark morphology, we have confirmed the absence of phase sensitivity by contrasting the performance of the two morphologies in EOC (Supporting Information **Figure S13**). The comparison in terms of titanium-specific space time yields to the targeted CH_3X or C_2H_4 evidenced up to three times higher values in all reactions (**Figure 4**), reaching 0.6 *versus* 0.2 mol_{CH_3X} h^{-1} mol_{Ti}^{-1} in MOC and MOB, and 2.5 *versus* 0.7 $mol_{C_2H_4}$ h^{-1} mol_{Ti}^{-1} in EOC and EOB. In terms of product distribution, the composite exhibited enhanced selectivity to the desired CH_3X or C_2H_4 compared to TiO_2. Particularly, in the case of MOC TiC-SiC yielded CH_3Cl (S_{CH_3Cl} = 40-50%), whereas TiO_2 selectively produced CO ($S_{CO} \leq 90\%$) from the oxidation of CH_3Cl as previously reported.[21] In MOB, TiC-SiC showed also higher selectivity to CH_3Br compared to TiO_2 particularly at low temperatures. In EOC, the selectivity to C_2H_4 increased over TiC-SiC upon increasing the temperature whereas it slightly decreased for TiO_2, ultimately converging to similar values, *i.e.* 84%, at the highest temperature investigated. On the other hand, TiC-SiC showed higher selectivities to C_2H_4 than TiO_2 in EOB, *i.e.*, 65% versus 45%, respectively.

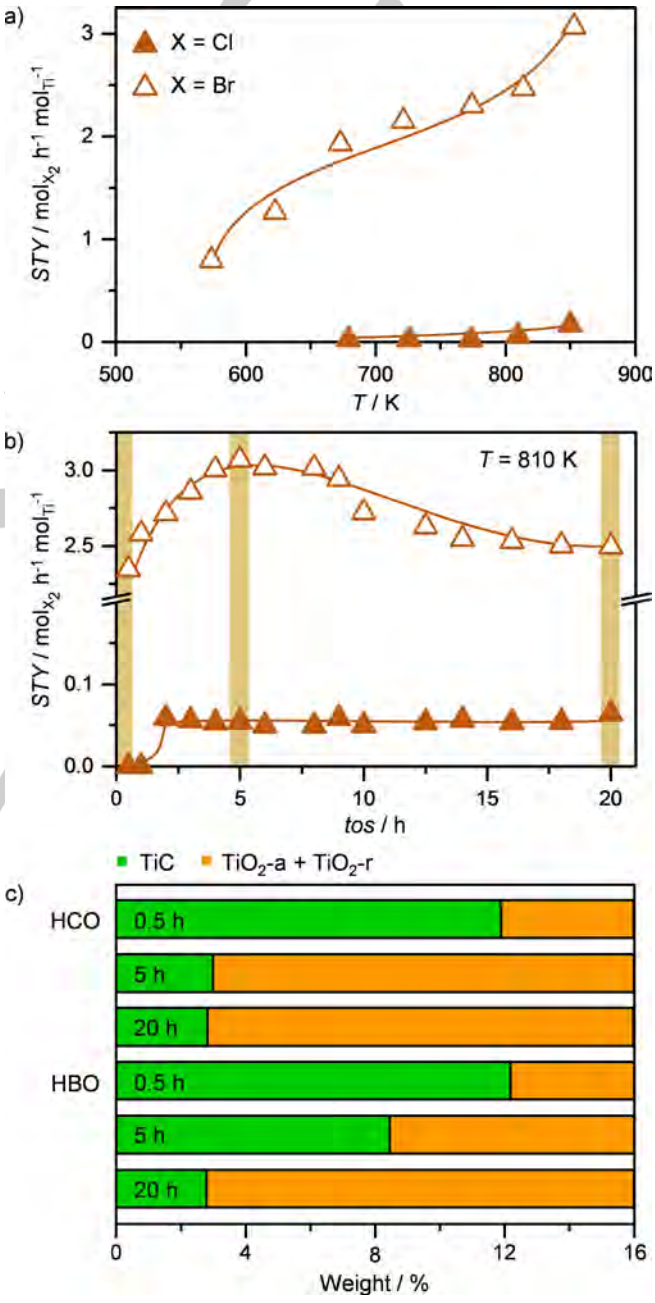

Figure 7. Space-time-yield of molecular halogen as a function of **a)** temperature or **b)** time-on-stream (*tos*) in HCO and HBO over TiC-SiC. The yellow boxes represent the different *tos* in HCO and HBO when the activated TiC-SiC were sampled for characterization. **c)** Quantification of the TiC and TiO_2 phases derived from TGA analysis. The TGA profiles are provided in **Figure S10** of the Supporting Information.

To assess the impact of the *in situ* generated active phase in the SiC matrix on the observed performance, a physical mixture of TiO_2 and SiC (TiO_2-SiC-pm) with the same titanium loading as in the composite was evaluated in EOC (**Figure 4b**). The resulting mixture showed lower activity than TiC-SiC and significant differences in the product distribution (Supporting Information **Figure S6**). Indeed, despite the occurrence of similar oxychlorination-dehydrochlorination consecutive pathways in both cases, TiO_2-SiC-pm displayed much lower selectivity to the desired C_2H_4 than the composite ($S_{C_2H_4} \leq 40\%$ *versus* $\leq 82\%$) and higher selectivity to the C_2H_5Cl intermediate ($S_{C_2H_5Cl} \leq 65\%$ *versus* $\leq 20\%$). These results suggest the beneficial effect of the embedment of the *in situ* generated TiO_2 in the thermally conductive SiC matrix. By comparing to the best benchmark catalysts, *i.e.* CeO_2 for MOC[19,22] and EuOX for both MOB[20] and EOC,[23] the performance of TiC-SiC was inferior. Nevertheless, this material represents an interesting alternative owing to its high thermal conductivity, low price particularly in relation to EuOX, and its availability as a commercial technical catalyst.

Conclusions

TiC-SiC composite was found to be active and selective in the oxyhalogenation of alkanes for natural gas upgrading, which represents the first application of this material as effective heterogeneous oxidation catalyst. The selectivity to methyl halides in methane oxychlorination (*ca.* 50%) and oxybromination (*ca.* 85%) surpassed that of reference TiO_2 anatase (*ca.* 30 and 70%, respectively). Similarly, in ethane oxybromination the composite reached *ca.* 70% selectivity to ethylene *versus* 45% obtained over TiO_2 anatase, whereas analogous selectivities to ethylene (*ca.* 85%) were attained in ethane oxychlorination. With respect to titanium, up to three times higher space time yields to the targeted product were observed in all reactions. Based on extensive characterization, this behavior was attributed to the *in situ* formation of the active phase *via* the selective partial oxidation of TiC into TiO_2. The latter remained embedded within the thermally conductive SiC matrix, facilitating heat dissipation, which seems beneficial for the superior selectivity as evidenced by the comparison with the reference physical mixture of TiO_2 anatase and SiC in ethane oxychlorination (*ca.* 85% *versus* 40% selectivity to ethylene). Assessment of the kinetics of the activation process of the composite in HCl and HBr oxidation revealed a progressive transformation of a fraction of TiC into TiO_2 concurrent with the stabilization of the activity. In addition to providing new insights on the structure and morphological characteristics of TiC-SiC composites, the findings highlight the potential of this catalyst for selective natural gas upgrading, thus inspiring future studies over this material for novel catalytic applications.

Experimental Section

Materials. The commercial TiC-SiC composite used in this work was synthesized by SICAT GmbH & Co. (TiC-SiC-E3-HP, 16.0 wt.% Ti, extrudate form) using a modified Ledoux method,[29] in which TiO_2-P25, Si, and C precursors are reacted at 1600 K under an argon atmosphere to allow the carburization and siliconation reactions to occur. The as-received TiC-SiC extrudates were crushed, sieved to the desired average particle size (d_p = 0.4-0.6 mm), and used as such in the catalytic tests. Commercial TiO_2 anatase (Sigma-Aldrich, anatase nanopowder, 99.5%) and rutile (Sigma-Aldrich, rutile nanopowder, 99.5%) were calcined at 873 K for 5 h (5 K min^{-1}) prior to use. The same TiO_2 anatase was used to prepare a physical mixture with SiC (SICAT, SiC-E3-HP), denoted as TiO_2-SiC-pm, with the same Ti content as in the TiC-SiC composite.

Characterization. X-ray diffraction (XRD) patterns were acquired in a PANalytical X'Pert PRO-MPD diffractometer using Cu-Kα radiation (λ = 0.154 nm). The data was recorded in the 10-70° 2θ range with an angular step size of 0.017° and a counting time of 4.1 s per step. N_2 sorption at 77 K was measured in a Micromeritics TriStar II analyzer. Prior to the measurements, the samples were evacuated at 573 K for 3 h. X-ray fluorescence spectroscopy (XRF) was used to quantify the Ti content by using an Orbis Micro instrument equipped with a Rh source operated at 35 kV and 500 μA. Thermogravimetric analysis (TGA) was performed using a Mettler-Toledo TGA/DSC 1 Star system. The solid was pretreated in flowing air (45 cm^3 min^{-1}) at 393 K for 2 h followed by heating (5 K min^{-1}) in the same atmosphere to 1223 K. Temperature-programmed reduction with hydrogen (H_2-TPR) and oxidation with O_2 (O_2-TPO) were performed in a Micromeritics Autochem II 2920 analyzer coupled with a OmniStar quadrupole mass spectrometer (MS). In both analyses, the solid was loaded into a U-shaped quartz micro-reactor, pretreated in He (20 cm^3 min^{-1}) at 473 K for 1 h, and cooled to 323 K. The H_2-TPR analysis was carried out in 5 vol.% of H_2 in N_2 (20 cm^3 min^{-1}), ramping the temperature from 323 K to 1273 K at a heating rate of 10 K min^{-1}. For O_2-TPO analysis, the samples were heated in a mixture comprising 20 vol.% O_2 in He (20 cm^3 min^{-1}) to 1273 K at 10 K min^{-1}. Scanning transmission electron (STEM) micrographs were acquired on a Talos F200X instrument operating at 200 kV and equipped with a high-angle annular dark-field (HAADF) detector as well as an energy-dispersive X-ray spectrometer (EDX). X-ray photoelectron spectroscopy (XPS) was conducted using a Physical Electronics (PHI) Quantum 2000 X-ray photoelectron spectrometer featuring monochromatic Al Kα radiation, generated from an electron beam operated at 15 kV and 32.3 W. The energy scale of the instrument was calibrated using Au and Cu reference samples. The samples were firmly pressed onto indium foil patches, which were then mounted onto a sample plate and introduced into the spectrometer. The analysis was conducted at 1×10^{-6} Pa, with an electron take off angle of 45° and a pass energy of 23.50 eV. Charge compensation during the measurement was achieved using a low energy electron source. The spectra were then shifted by aligning the main component of the C 1*s* core level spectra to 284.8 eV. Surface elemental concentrations were determined in atomic percent using the measured photoelectron peak areas after Shirley background subtraction and the built-in sensitivity factors for calculation. Fits of the Ti 2*p*, C 1*s* and Si 2*p* core level spectra were performed for a qualitative comparison of the samples. Binding energy ranges and boundary conditions for the fits were chosen according to the literature.[38] Solid-state magic angle spinning nuclear magnetic resonance (MAS NMR) spectra of ^{29}Si and ^{13}C were recorded at a spinning speed of 10 kHz on a Bruker Avance 400 MHz spectrometer featuring a 4 mm probe head and 4 mm ZrO_2 rotors. ^{29}Si MAS NMR spectra were collected using 1024 accumulations, 90° pulses with a length of 4 μs, a recycle delay of 10 s, and tetramethylsilane as reference. For ^{13}C MAS NMR spectra, 1024 accumulations, 90° pulses with a length of 2.7 μs, a recycle delay of 10 s, and glycine as reference were used. Raman spectroscopy was carried out in a confocal Raman microscope (WITec CRM 200) using a 532 nm diode laser. The microscope was operated in the backscattering mode with a 100x objective lens and 6 mW power.

Catalytic tests. Activation of the TiC-SiC composite was performed under methane and ethane oxychlorination/oxybromination and HCl and HBr oxidation conditions at ambient pressure in a continuous-flow fixed-bed reactor setup, which is detailed elsewhere.[22,23] The gases CH_4 (PanGas, purity 5.5), C_2H_6 (PanGas, purity 3.5), HCl (Air Liquide, purity 2.8, anhydrous), HBr (Air Liquide, purity 2.8, anhydrous), O_2 (PanGas, purity 5.0), Ar (PanGas, purity 5.0; internal standard), and He (PanGas, purity 5.0; carrier gas), were fed by digital mass flow controllers (Bronkhorst®) to achieve a total volumetric flow, F_T, of 6 L STP h^{-1}, containing a stoichiometric mixture (alkane:HX:O_2:Ar:He = 6:6:3:4.5:80.5; X = Cl, Br). In the case of HCl and HBr oxidation, the feed composition used was HX:O_2:He = 6:3:91. A quartz reactor (10 mm internal diameter) was loaded with the catalyst (catalyst weight, W_{cat} = 1 g, particle size, d_p = 0.4-0.6 mm), and placed in an electrical oven. A K-type thermocouple fixed in a coaxial quartz thermowell with the tip positioned in the center of the catalyst bed was used to monitor the temperature during the reaction. Prior to testing, the catalyst bed was heated in a He flow to the desired temperature (T = 523-850 K) and allowed to stabilize for at least 30 min before the reaction mixture was fed. The down-stream lining was heated at 393 K to prevent the condensation of reaction products. The effluent gas stream was sent through impinging bottles containing an aqueous 1 M NaOH solution for neutralization prior to release to the ventilation system. Quantification of X_2 was performed by its absorption in an impinging bottle filled with an aqueous 0.1 M KI solution ($X_2 + 3I^- \rightarrow I_3^- + 2X^-$) followed by iodometric titration (Mettler Toledo G20 Compact Titrator) of the formed triiodide ($I_3^- + 2S_2O_3^{2-} \rightarrow 3I^- + S_4O_6^{2-}$) with an aqueous 0.01 M $Na_2S_2O_3$ solution (Aldrich, 99.99%). Carbon-containing compounds (CH_4, C_2H_6, C_2H_4, CH_3X, CH_2X_2, C_2H_5X, CO, and CO_2) and Ar were quantified using an on-line gas chromatograph equipped with a GS-Carbon PLOT column coupled to a mass spectrometer (GC-MS, Agilent GC 6890, Agilent MSD 5973N).

The conversion of reactant i, X_i, (i: CH_4, or C_2H_6) was calculated using Eq. 1,

$$X_i = \frac{n_i^{inlet} - n_i^{outlet}}{n_i^{inlet}} \times 100, \% \quad \text{Eq. 1}$$

where n_i^{inlet} and n_i^{outlet} are the respective molar flows of the reactant i at the reactor inlet and outlet.

The conversion of HX, X_{HX}, was calculated according to Eq. 2,

$$X_{HX} = \frac{2 \times n_{X_2}^{outlet}}{n_{HX}^{inlet}} \times 100, \% \quad \text{Eq. 2}$$

where $n_{X_2}^{outlet}$ and n_{HX}^{inlet} denote the respective molar flows of X_2 and HX at reactor outlet and inlet.

The reaction rate expressed with respect to the reactant i, r_i (i: CH_4, C_2H_6, or HX) and based on the titanium content was calculated using Eq. 3,

$$r_i = \frac{n_i^{inlet} - n_i^{outlet}}{W_{cat} \times x_{Ti}} \times MW_{cat}, \text{ mol}_i \text{ h}^{-1} \text{ mol}_{Ti}^{-1} \quad \text{Eq. 3}$$

where MW_{cat} and x_{Ti} are the catalyst molecular weight and molar titanium content, respectively.

The selectivity to product j, S_j, and the yield and space-time-yield of product j, Y_j, and STY_j (j: CH_4, C_2H_4, CH_3X, CH_2X_2, C_2H_5X, CO, and CO_2) were calculated using Eqs. 4, 5, and 6, respectively,

$$S_j = \frac{n_j^{outlet} \times N_{C,j}}{\sum n_j^{outlet} \times N_{C,j}} \times 100, \% \quad \text{Eq. 4}$$

$$Y_j = \frac{X_i \times S_j}{100}, \% \quad \text{Eq. 5}$$

$$STY_j = \frac{n_j^{outlet}}{W_{cat} \times x_{Ti}} \times MW_{cat}, \text{ mol}_j \text{ h}^{-1} \text{ mol}_{Ti}^{-1} \quad \text{Eq. 6}$$

where n_j^{outlet} is the molar flow of the product j at the reactor outlet and $N_{C,j}$ is the number of carbon atoms in the compound j.

The error of the carbon mass balance, ε_C, determined using Eq. 7,

$$\varepsilon_C = \frac{n_i^{inlet} \times N_{C,i} - \left(n_i^{outlet} \times N_{C,i} + \sum n_j^{outlet} \times N_{C,j}\right)}{n_i^{inlet} \times N_{C,i}} \times 100, \% \quad \text{Eq. 7}$$

was less than 5% in all experiments. All the catalysts were activated in the reaction mixture for a total time of 5 h and at a final temperature of 850 K. Additionally, the activation of the TiC-SiC composite in HBr and HCl oxidation at 810 K was monitored with time up to 20 h. After the tests, the reactor was quenched to room temperature in He flow and the catalyst was retrieved for *ex situ* characterization.

Acknowledgements

This work was supported by ETH Research Grant ETH-04 16-1 and by the Swiss National Science Foundation (project no. 200021-156107). The authors thank Prof. Ralph Spolenak and ScopeM at ETH Zurich for using their facilities. Micha Calvo and Dr. Réne Verel are acknowledged for Raman and NMR analyses, respectively.

Keywords: alkane oxyhalogenation • natural gas upgrading • C−H activation • titanium carbide-silicon carbide composite • titanium oxide

[1] J. J. H. B. Sattler, J. Ruiz-Martinez, E. Santillian-Jimenez, B. M. Weckhuysen, *Chem. Rev.* **2014**, *114*, 10613-10653.
[2] H. Schwarz, *Angew. Chem.* **2011**, *123*, 10276-10297; *Angew. Chem. Int. Ed.* **2011**, *50*, 10096-10115.
[3] E. V. Kondratenko, T. Peppel, D. Seeburg, V. A. Kondratenko, N. Kalevaru, A. Martin, S. Wohlrab, *Catal. Sci. Technol.* **2017**, *7*, 366-381.
[4] E. McFarland, *Science* **2012**, *338*, 340-342.
[5] J. A. Labinger, J. E. Bercaw, *Nature* **2002**, *417*, 507-514.
[6] R. Khalilpour, I. A. Karimi, *Energy* **2012**, *40*, 317-328.
[7] R. Lin, A. P. Amrute, J. Pérez-Ramírez, *Chem. Rev.* **2017**, *117*, 4182-4247.
[8] J. Tollefson, *Nature* **2016**, https://doi.org/10.1038/nature.2016.19141.
[9] U.S. Energy Information Administration, *Monthly Energy Review, June 2016*, U.S. Department of Energy, Washington, U.S., **2016**.
[10] R. Horn, R. Schlögl, *Catal. Lett.* **2015**, *145*, 23-39.
[11] D. A. Goetsch, L. D. Schmidt, *Science* **1996**, *271*, 1560-1562.
[12] A. S. Bodke, D. A. Olschki, L. D. Schmidt, E. Ranzi, *Science* **1999**, *285*, 712-715.
[13] F. Cavani, N. Ballarini, A. Cericola, *Catal. Today* **2007**, *127*, 113-131.
[14] C. A. Gärtner, A. C. van Veen, J. A. Lercher, *ChemCatChem* **2013**, *5*, 3196-3217.
[15] J. Oliver-Meseguer, A. Doménech-Carbó, M. Boronat, A. Leyva-Pérez, A. Corma, *Angew. Chem.* **2017**, *129*, 6535-6539; *Angew. Chem. Int. Ed.* **2017**, *56*, 6435-6439.
[16] M. J. Dagani, H. J. Barda, T. J. Benya, D. C. Sanders, *Ullmann's Encyclopedia of Industrial Chemistry*, *Vol. 6*, Wiley-VCH, Weinheim, **2012**, pp. 331-358.
[17] GTC Technology, 2017. Gas to Aromatics—GT-G2A℠. http://www.gtctech.com, accessed November 23rd, **2017**, 10:00 GMT.

[18] A. Leyva-Pérez, D. Cómbita-Merchánt, J. R. Cabrero-Antonino, S. I. Al-Resayes, A. Corma, *ACS Catal.* **2013**, *3*, 250-258.

[19] J. He, T. Xu, Z. Wang, Q. Zhang, W. Deng, Y. Wang, *Angew. Chem.* **2012**, *124*, 2488-2492; *Angew. Chem. Int. Ed.* **2012**, *51*, 2438-2442.

[20] V. Paunović, R. Lin, M. Scharfe, A. P. Amrute, S. Mitchell, R. Hauert, J. Pérez-Ramírez, *Angew. Chem.* **2017**, *129*, 9923-9927; *Angew. Chem. Int. Ed.* **2017**, *56*, 9791-9795.

[21] V. Paunović, G. Zichittella, R. Verel, A. P. Amrute, J. Pérez-Ramírez, *Angew. Chem.* **2016**, *128*, 15848-15852; *Angew. Chem. Int. Ed.* **2016**, *55*, 15619-15623.

[22] G. Zichittella, V. Paunović, A. P. Amrute, J. Pérez-Ramírez, *ACS Catal.* **2017**, *7*, 1805-1817.

[23] G. Zichittella, N. Aellen, V. Paunović, A. P. Amrute, J. Pérez-Ramírez, *Angew. Chem.* **2017**,*129*, 13858-13862; *Angew. Chem. Int. Ed.* **2017**, *56*, 13670-13674.

[24] H. Yamashita, Y. Nishida, S. Yuan, K. Mori, M. Narisawa, Y. Matsumura, T. Ohmichi, I. Katayama, *Catal. Today* **2007**, *120*, 163-167.

[25] Y. Liu, B. de Tymowski, F. Vigneron, I. Florena, O. Ersen, C. Meny, P. Nguyen, C. Pham, F. Luck, C. Pham-Huu, *ACS Catal.* **2013**, *3*, 393-404.

[26] M. J. Henderson, A. Gibaud, J.-F. Bardeau, J. W. White, *J. Mater. Chem.* **2006**, *16*, 2478-2484.

[27] Y. Chen, H. Zhang, D. Ma, J. Ma, H. Ye, G. Qi, Y. Ye, *Mater. Res. Bull.* **2011**, *46*, 1800-1803.

[28] M. Zhou, P. Don D. Rodrigo, X. Wang, J. Hu, S. Dong, Y.-B. Cheng, *J. Eur. Ceram. Soc.* **2014**, *34*, 1949-1954.

[29] P. Nguyen, C. Pham, *Appl. Catal., A* **2011**, *391*, 443-454.

[30] M. Moser, I. Czekaj, N. López, J. Pérez-Ramírez, *Angew. Chem.* **2014**, *126*, 8772-8777; *Angew. Chem. Int. Ed.* **2014**, *53*, 8628-8633.

[31] B. H. Lohse, A. Calka, D. Wexler, *J. Alloys Compd.* **2007**, *434-435*, 405-409.

[32] I.-K. Sung, C. M. Mitchell, D.-P. Kim, P. J. A. Kenis, *Adv. Funct. Mat.* **2005**, *15*, 1336-1342.

[33] M. M. Rahman, C. Y.-W. Yang, G. L. Harris in *Amorphous and Crystalline Silicon Carbide II*, Springer, Berlin, **1989**, pp. 68.

[34] J. S. Hartman, M. F. Richardson, B. L. Sherriff, B. G. Winsborrow, *J. Am. Chem. Soc.* **1987**, *109*, 6059-6067.

[35] K. MacKenzie, M.E. Smith in Multinuclear Solid-State Nuclear Magnetic Resonance of Inorganic Materials, Pergamon, Oxford, **2002**, pp. 256.

[36] X. Chen, S. S. Mao, *Chem. Rev.* **2007**, *107*, 2891-2959.

[37] M. Moser, V. Paunović, Z. Guo, L. Szentmiklósi, M.G. Hevia, M. Higham, N. López, D. Teschner, J. Pérez-Ramírez, *Chem. Sci.* **2016**, *7*, 2996-3005.

[38] V. Schier, H.-J. Michel, J. Halbritter, *Fresenius J. Anal. Chem.* **1993**, *346*, 227-232.

WILEY-VCH

FULL PAPER

TiC-SiC composite is shown for the first time as a high-performance catalyst for selective natural gas upgrading *via* oxyhalogenation chemistry. This is attributed to the *in situ* activation of TiC into TiO_2 phase, which remains embedded into the thermally conductive SiC matrix, facilitating heat dissipation, thus improving selectivity control.

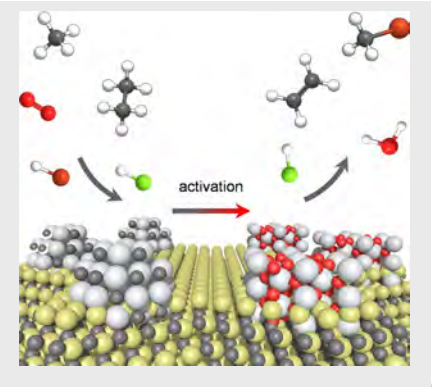

*G. Zichittella, B. Puértolas, S. Siol, V. Paunović, S. Mitchell, J. Pérez-Ramírez**

Page No. – Page No.

Activated TiC-SiC Composite for Natural Gas Upgrading *via* Catalytic Oxyhalogenation

Table S1. Surface composition determined by X-ray photoelectron measurements of the TiC-SiC composite in fresh form and after activation in ethane oxychlorination (EOC) and oxybromination (EOB), and in the oxidation of HCl (HCO) and HBr (HBO) at different time-on-stream.

Sample	Ti content / at.%	Si content / at.%	O content / at.%	C content / at.%
Fresh	1.3	26.0	23.8	48.9
EOC	1.6	30.0	48.1	20.3
EOB	2.2	23.4	26.2	48.2
HCO 0.5 h	1.7	29.4	35.4	33.5
HCO 20 h	1.5	31.1	47.6	19.7
HBO 0.5 h	2.3	27.0	35.7	35.0
HBO 5 h	1.8	32.4	47.3	18.6

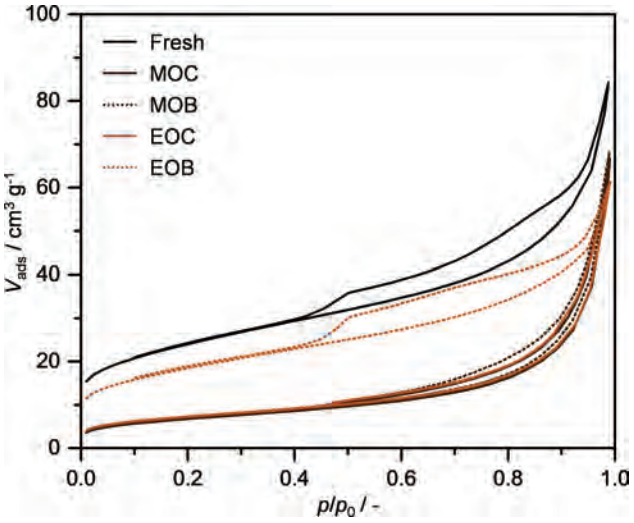

Figure S1. N_2 sorption isotherms at 77 K of TiC-SiC in fresh form and after activation in methane oxychlorination (MOC) and oxybromination (MOB), and ethane oxychlorination (EOC) and oxybromination (EOB).

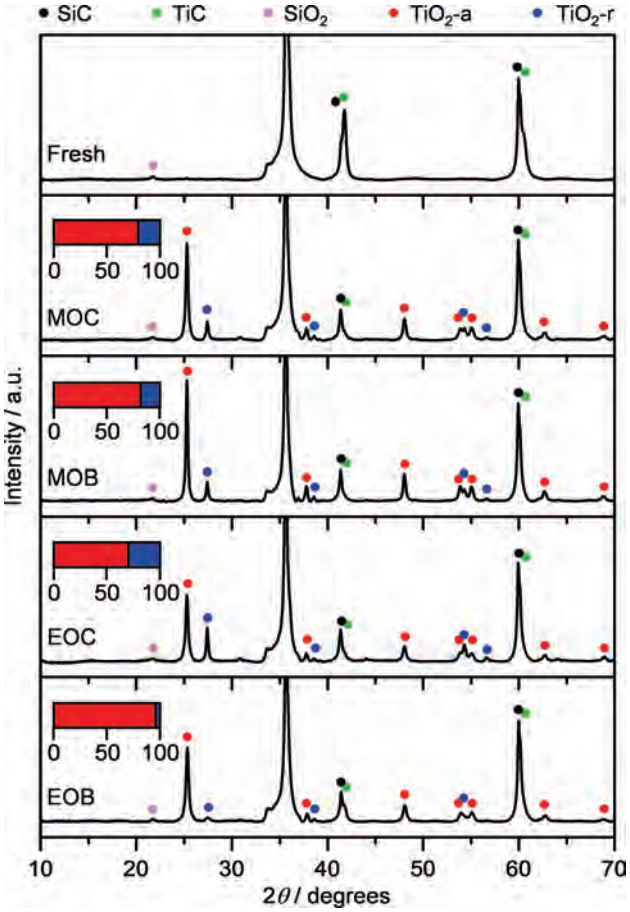

Figure S2. X-ray diffractograms of TiC-SiC in fresh form and after activation in methane oxychlorination (MOC) and oxybromination (MOB), and ethane oxychlorination (EOC) and oxybromination (EOB). The insets indicate the proportions in area % of the anatase (TiO_2-a; red) and rutile (TiO_2-r; blue) phases of titania in the activated catalysts.

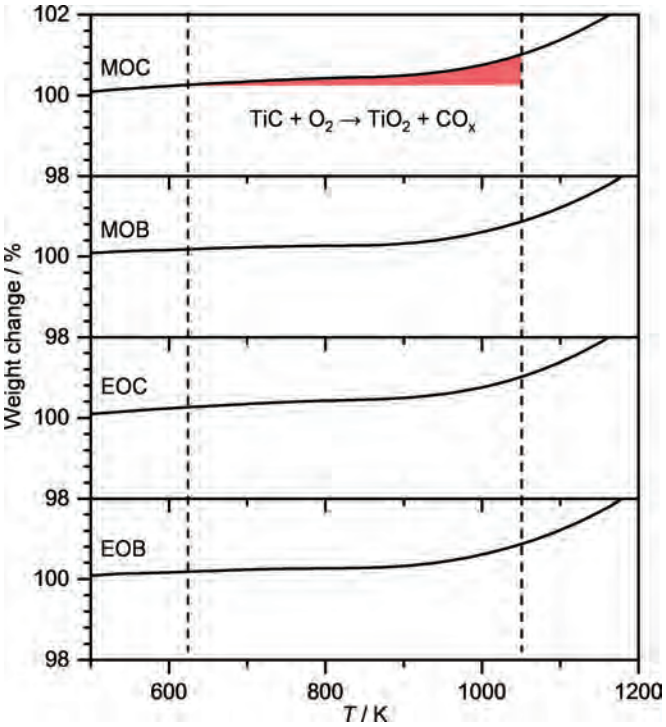

Figure S3. Thermogravimetric analysis (TGA) in air of TiC-SiC after activation in methane oxychlorination (MOC) and oxybromination (MOB), and ethane oxychlorination (EOC) and oxybromination (EOB). Quantification of the remaining TiC in the activated samples was assessed by integrating the TGA profile (light red area) in the region between *ca.* 600 K and 1000 K where the oxidation of TiC occurs, as exampled for MOC. These results are shown in **Figure 1** of the main manuscript.

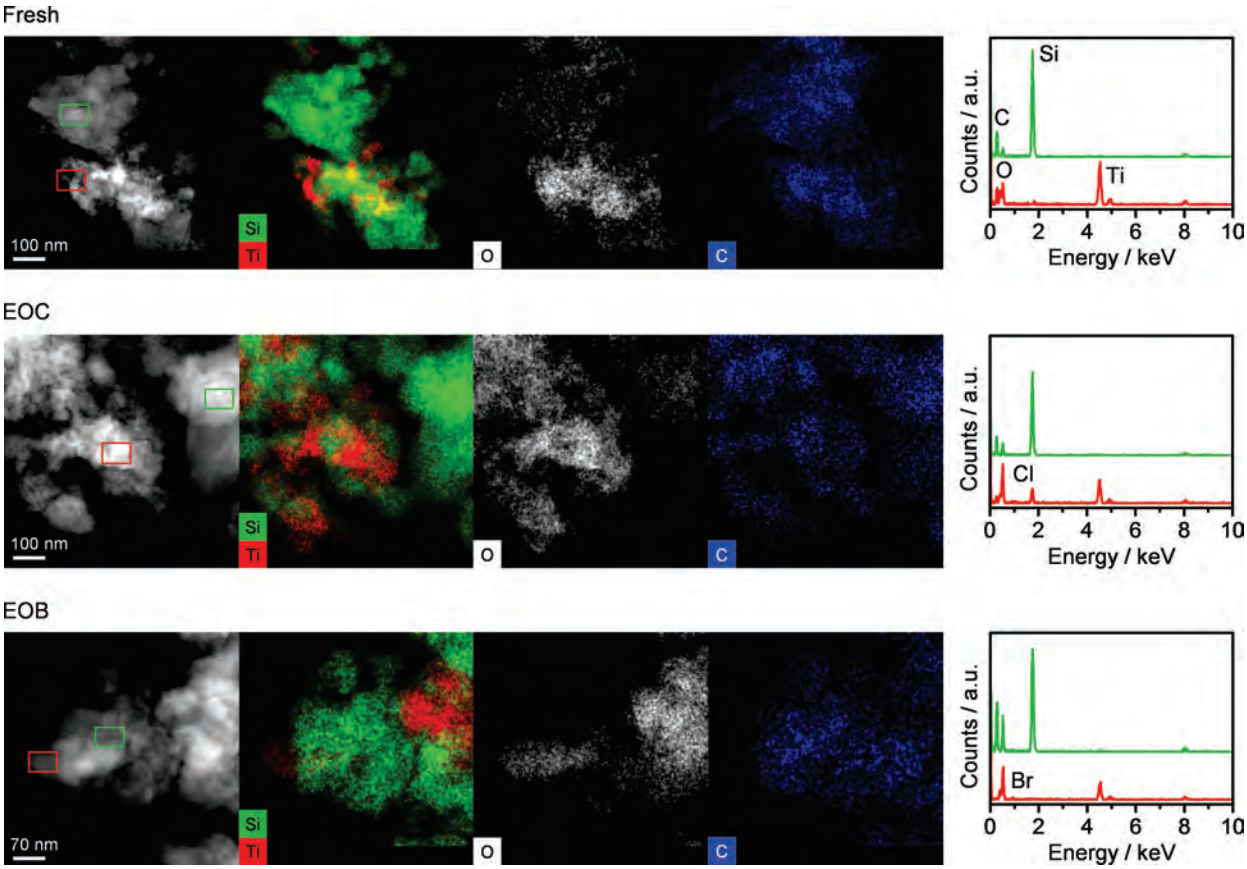

Figure S4. Scanning transmission electron micrographs acquired in high-angle annular dark field mode and corresponding elemental maps of TiC-SiC in fresh form and after activation in ethane oxychlorination (EOC), and oxybromination (EOB). The energy-dispersive X-ray spectra corresponding to the boxed Si (green box) and Ti (red box) rich regions are shown at the right of the micrographs.

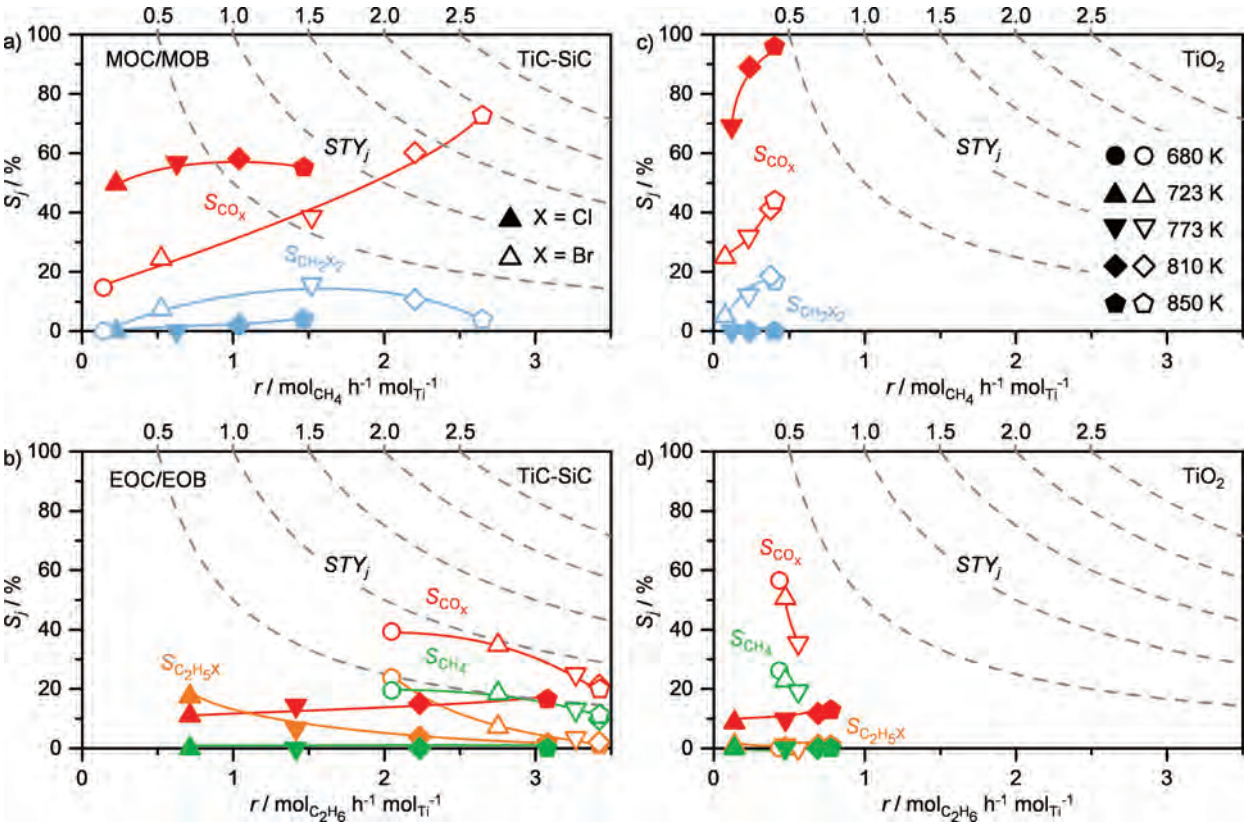

Figure S5. Selectivity to product *j* as a function of the rate of alkane consumption in the oxychlorination (solid symbols) and oxybromination (open symbols) of **a)**, **c)** methane (MOC/MOB), and **b)**, **d)** ethane (EOC/EOB) over TiC-SiC and TiO_2. The selectivity to CH_3X or C_2H_4 (desired products) is shown in **Figure 4** of the main manuscript. The dashed gray lines indicate the space-time-yield of product *j* in $mol_j\ h^{-1}\ mol_{Ti}^{-1}$ and the different symbols refer to the reaction temperature. In case of EOC and EOB, no dihaloethanes were observed in the temperature window investigated. Feed composition: alkane:HX:O_2:Ar:He = 6:6:3:4.5:80.5.

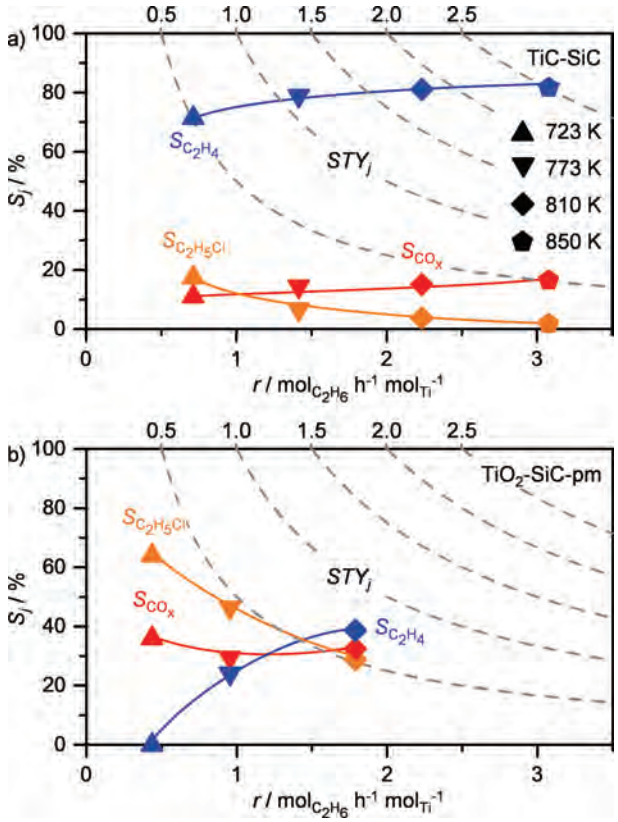

Figure S6. Selectivity to product *j* as a function of the rate of ethane consumption in the oxychlorination of ethane over **a)** TiC-SiC and **b)** a physical mixture of TiO_2 and SiC (TiO_2-SiC-pm) with the same Ti content (16 wt.%). The dashed gray lines indicate the space-time-yield of product *j* in mol_j h^{-1} mol_{Ti}^{-1} and the different symbols refer to the reaction temperature. Feed composition: C_2H_6:HCl:O_2:Ar:He = 6:6:3:4.5:80.5.

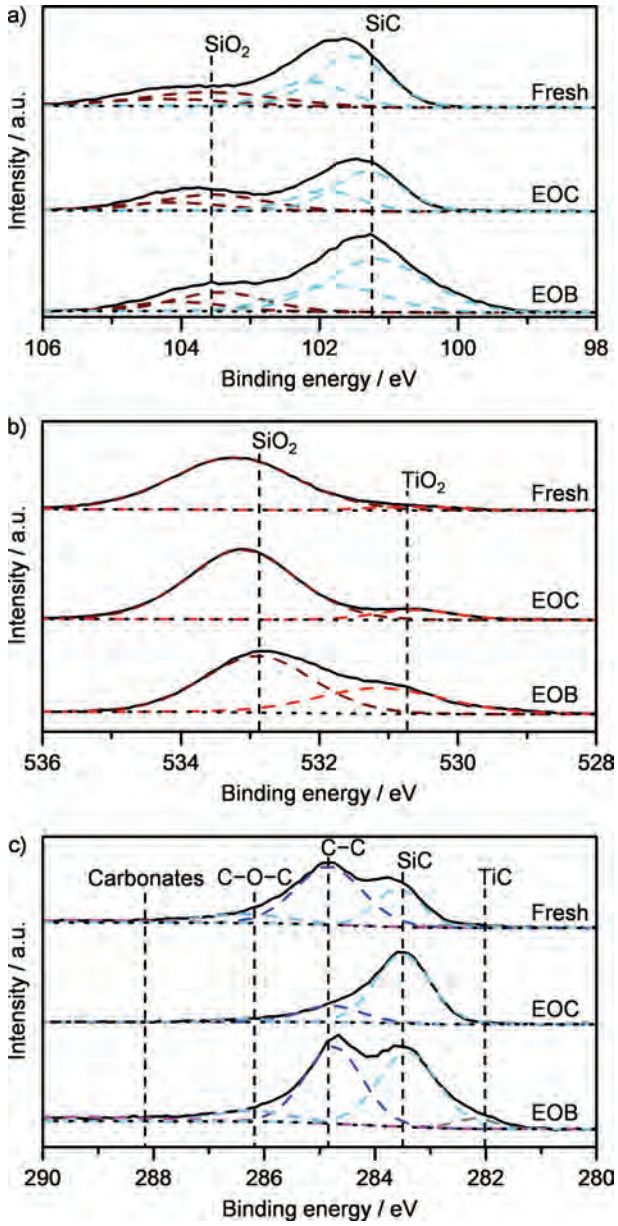

Figure S7. a) Si 2*p*, **b)** O 1*s*, and **c)** C 1*s* core level spectra of TiC-SiC in fresh form and after activation in ethane oxychlorination (EOC) and oxybromination (EOB) as shown in **Figure 4** of the main manuscript. The solid, dotted, and dashed lines represent the raw data, background, and fits of the different contributions, respectively. The Ti 2*p* core level spectra is presented in **Figure 5** of the main manuscript. SiC and TiC reference binding energies have been assigned according to literature (Schier *et al*., *Fresenius J. Anal. Chem.* **1993**, *346*, 227-232).

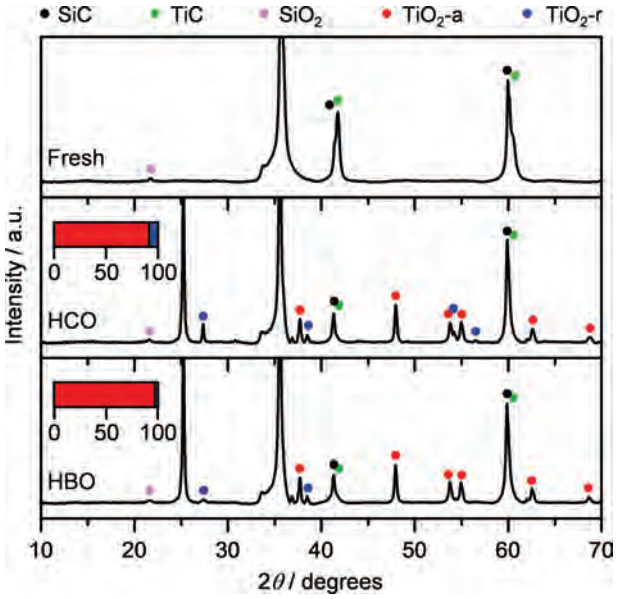

Figure S8. X-ray diffractograms of TiC-SiC in fresh form and after activation in the oxidation of HCl (HCO) and HBr (HBO) as shown in **Figure 7** of the main manuscript. The insets indicate the proportions in area % of the anatase (TiO_2-a; red) and rutile (TiO_2-r; blue) phases of titania in the activated catalysts.

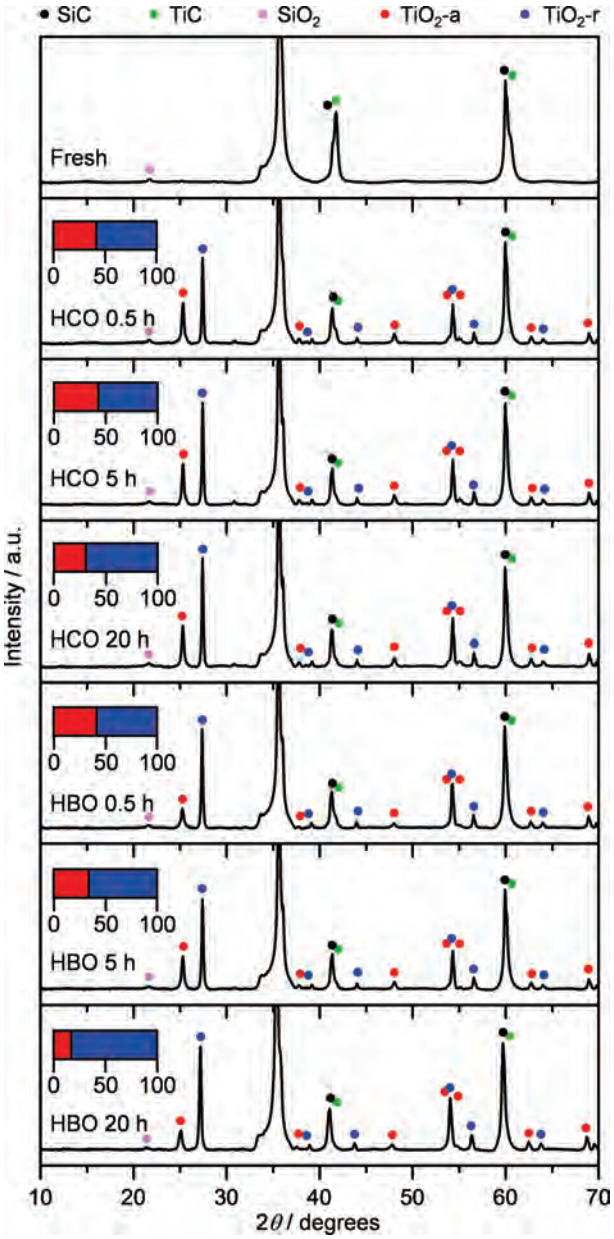

Figure S9. X-ray diffractograms of TiC-SiC in fresh form and after activation in the oxidation of HCl (HCO) and HBr (HBO) at different time-on-stream as shown in **Figure 7** of the main manuscript. The insets indicate the proportions in area % of the anatase (TiO_2-a; red) and rutile (TiO_2-r; blue) phases of titania in the activated catalysts.

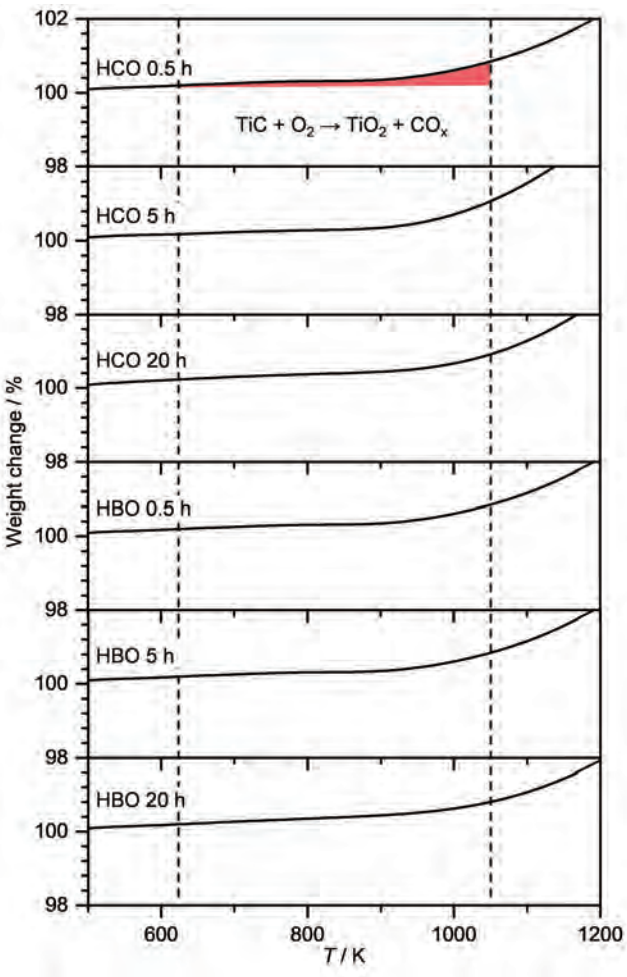

Figure S10. Thermogravimetric analysis (TGA) in air of TiC-SiC after activation in the oxidation of HCl (HCO) and HBr (HBO) at different time-on-stream as shown in **Figure 7** of the main manuscript. Quantification of the remaining TiC in the activated samples was assessed by integrating the TGA profile (light red area) in the region between *ca*. 600 K and 1000 K where the oxidation of TiC occurs, as exampled for HCO 0.5 h. These results are shown in **Figure 7** of the main manuscript.

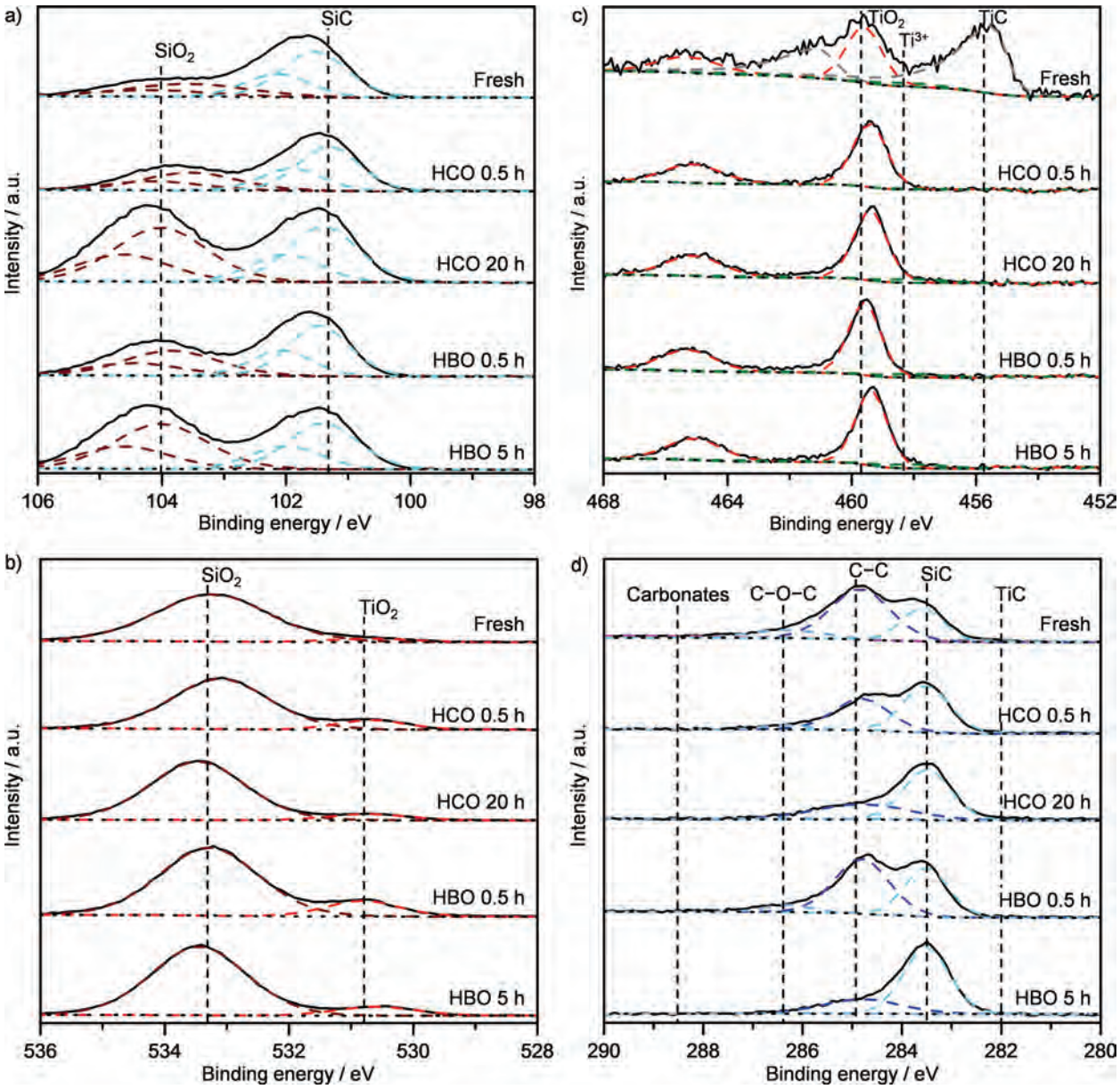

Figure S11. a) Si 2*p*, **b)** O 1*s*, **c)** Ti 2*p*, and **d)** C 1*s* core level spectra of TiC-SiC in fresh form and after activation in the oxidation of HCl (HCO) and HBr (HBO) at different time-on-stream as shown in **Figure 7** of the main manuscript. The solid, dotted, and dashed lines represent the raw data, background, and fits of the different contributions, respectively. SiC and TiC reference binding energies have been assigned according to literature (Schier *et al.*, *Fresenius J. Anal. Chem.* **1993**, *346*, 227-232).

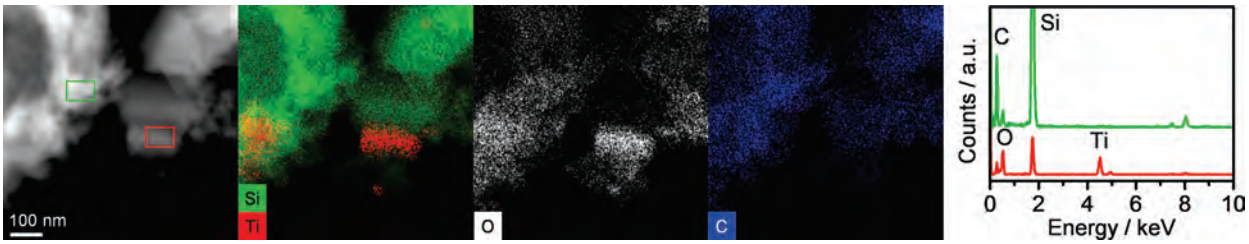

Figure S12. Scanning transmission electron micrographs acquired in high-angle annular dark field mode and corresponding elemental maps of TiC-SiC after activation for 0.5 h on stream under HBr oxidation conditions as shown in **Figure 7** of the main manuscript. The energy-dispersive X-ray spectra corresponding to the boxed Si (green box) and Ti (red box) rich regions are shown at the right of the micrographs.

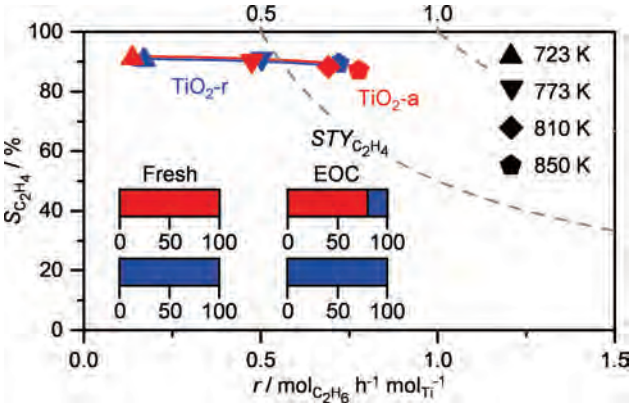

Figure S13. Selectivity to C_2H_4 as a function of the rate of alkane consumption in the oxychlorination of ethane (EOC) over the anatase (TiO_2-a; red) and rutile (TiO_2-r; blue) phases of TiO_2. The dashed gray lines indicate the space-time-yield of C_2H_4 in $mol_{C_2H_4}\ h^{-1}\ mol_{Ti}^{-1}$ and the different symbols refer to the reaction temperature. Feed composition: C_2H_6:HCl:O_2:Ar:He = 6:6:3:4.5:80.5. The insets indicate the proportions in area % of the anatase (TiO_2-a; red) and rutile (TiO_2-r; blue) phases of titania in the activated catalysts derived from X-ray diffraction analyses of the samples in fresh form and after EOC.